ADVANCED MATERIALS
www.advmat.de

Composition Engineering of Amorphous Nickel Boride Nanoarchitectures Enabling Highly Efficient Electrosynthesis of Hydrogen Peroxide

Jie Wu, Meilin Hou, Ziliang Chen, Weiju Hao, Xuelei Pan, Hongyuan Yang, Wanglai Cen, Yang Liu,* Hui Huang, Prashanth W. Menezes,* and Zhenhui Kang**

Developing advanced electrocatalysts with exceptional two electron ($2e^-$) selectivity, activity, and stability is crucial for driving the oxygen reduction reaction (ORR) to produce hydrogen peroxide (H_2O_2). Herein, a composition engineering strategy is proposed to flexibly regulate the intrinsic activity of amorphous nickel boride nanoarchitectures for efficient $2e^-$ ORR by oriented reduction of Ni^{2+} with different amounts of BH_4^-. Among borides, the amorphous NiB_2 delivers the $2e^-$ selectivity close to 99% at 0.4 V and over 93% in a wide potential range, together with a negligible activity decay under prolonged time. Notably, an ultrahigh H_2O_2 production rate of 4.753 mol g_{cat}^{-1} h^{-1} is achieved upon assembling NiB_2 in the practical gas diffusion electrode. The combination of X-ray absorption and in situ Raman spectroscopy, as well as transient photovoltage measurements with density functional theory, unequivocally reveal that the atomic ratio between Ni and B induces the local electronic structure diversity, allowing optimization of the adsorption energy of Ni toward *OOH and reducing of the interfacial charge-transfer kinetics to preserve the O—O bond.

1. Introduction

Hydrogen peroxide (H_2O_2) is one of the most important chemicals in the world and has been extensively deployed as a disinfectant, blench, and combustion improver.[1–4] The current synthesis of H_2O_2 mainly focuses on the anthraquinone process, which not only involves expensive catalysts and high gas pressures but also produces enormous energy consumption and organic wastes.[5–7] As an atomic economy, sustainable, and green method, the directional reduction of O_2 to H_2O_2 via electrocatalysis is a promising alternative to the conventional anthraquinone process.[8–10] However, the oxygen reduction reaction (ORR) inherently bears the high tendency to undergo the four electron ($4e^-$) transfer to form H_2O, which inevitably suppresses the formation of

J. Wu, Z. Chen, Y. Liu, H. Huang, Z. Kang
Institute of Functional Nano and Soft Materials (FUNSOM)
Jiangsu Key Laboratory for Carbon-Based Functional Materials and Devices
Soochow University
Suzhou 215123, P. R. China
E-mail: zlchen@suda.edu.cn; yangl@suda.edu.cn; zhkang@suda.edu.cn

M. Hou
College of Engineering
Hebei Normal University
Shijiazhuang 050024, P. R. China

Z. Chen, H. Yang, P. W. Menezes
Department of Chemistry: Metalorganics and Inorganic Materials
Technische Universität Berlin
Straße des 17 Juni 135, Sekr. C2, 10623 Berlin, Germany
E-mail: prashanth.menezes@mailbox.tu-berlin.de

The ORCID identification number(s) for the author(s) of this article can be found under https://doi.org/10.1002/adma.202202995.

DOI: 10.1002/adma.202202995

W. Hao
College of Science
University of Shanghai for Science and Technology
Shanghai 200093, P. R. China

X. Pan
State Key Laboratory of Advanced Technology for Materials Synthesis and Processing
Wuhan University of Technology
Wuhan 430070, P. R. China

X. Pan, W. Cen
Institute of New Energy and Low Carbon Technology
Sichuan University
Chengdu 610065, P. R. China

P. W. Menezes
Material Chemistry Group for Thin Film Catalysis – CatLab
Helmholtz-Zentrum Berlin für Materialien und Energie
Albert-Einstein-Str. 15, 12489 Berlin, Germany

H_2O_2 through two electron ($2e^-$) pathway.[11–14] In this regard, developing electrocatalysts with high $2e^-$ ORR selectivity is vitally important for the efficient production of H_2O_2.

Recently, several kinds of inexpensive transition metal-based compounds including oxides,[15–17] chalcogenides,[18–20] and phosphides[21–23] have been exploited for selective reduction of O_2 to H_2O_2, by which their huge potential as $2e^-$ ORR electrocatalysts has been eloquently confirmed. For instance, in 2021, Jiang et al. found that the $Cu_{72}Se_4$ delivered the $2e^-$ selectivity as high as 90%,[18] and following this observation, Zhao et al. in 2022 reported that the $2e^-$ selectivity for $Ni_{2-x}P$ could be reached higher than 92%.[21] To further enhance the selectivity, very recently, Menezes and his coworkers synthesized the high entropy perovskite oxides, which displayed a $2e^-$ selectivity up to 96%.[24] Not only these remarkable new findings are appealing but also they are inspiring others to search for more diverse transition metal-based (TM) electrocatalysts toward $2e^-$ ORR. To the best of our knowledge, nearly all reported electrocatalysts with outstanding $2e^-$ ORR activity is mainly focused on the crystalline phases. Nevertheless, it has been widely accepted now that as compared to the crystalline phases, the corresponding amorphous materials hold the short-range local symmetry, apparent unsaturated coordination atoms, and more abundant defects, which are expected to enhance the number of intrinsic active sites as well as induce the unique electronic structure, and thus providing the platform for optimizing the $2e^-$ ORR activity.[25–28] Based on this premise, it can be envisioned that the construction of amorphous TM-based electrocatalysts for $2e^-$ ORR is highly promising and intriguing for both fundamental and industrial applications. However, the relevant investigation on amorphous TM-based electrocatalysts has received limited interest, and such amorphous electrocatalysts concurrently integrating the merits of low cost and high performance with admirable $2e^-$ ORR activity, selectivity, and stability have never been reported so far. Furthermore, a deep understanding of their composition-electronic structure–activity could be crucial to driving efficient $2e^-$ ORR catalysis and therefore requires special attention.

Motivated by the above concerns, in this contribution, a series of amorphous nickel boride nanoarchitectures with different atomic ratios between Ni and B have been deliberately synthesized by one-pot reduction of Ni^{2+} using borohydride. The purpose of choosing nickel borides here is owing to their tunable composition, high intrinsic conductivity, multiple functions as well as the viable $2e^-$ ORR pathway.[29–36] The X-ray absorption spectra (XAS), in situ Raman spectra, transient photovoltage (TPV) measurements coupled with density functional theory (DFT) calculations unveiled that the variation of atomic ratio leads to the distinct electronic structure of nickel borides, which then alters both the adsorption free energy and adsorption model of active Ni site to the *OOH intermediate as well as the surface charge-transfer kinetics on their surface. The optimal amorphous NiB_2 nanoarchitectures exhibited the best H_2O_2 selectivity up to 99% at 0.4 V and more than 93% in a wide potential range from 0.2 to 0.6 V vs reversible hydrogen electrode (RHE). Furthermore, it could maintain the exceptional activity for 12 h with negligible decay, which surpassed recently reported state-of-art catalysts. Remarkably, when assembled as a gas diffusion electrode, NiB_2 delivered ultrahigh H_2O_2 productivity of 4.753 mol H_2O_2 g_{cat}^{-1} h^{-1} under a continuous operation of 12 h. The work presented here provides a new perspective on the development of high-performance amorphous catalysts for the reduction of O_2 to H_2O_2.

2. Results and Discussion

A series of nickel borides with different atomic ratios were synthesized by a spontaneous redox reaction in the presence of $NiSO_4$ and $NaBH_4$ aqueous solution under an ambient condition in a nitrogen atmosphere (see the Experimental section, Table S1, Supporting Information). The phase structure for these compounds was first assessed by X-ray diffraction (XRD). As shown in **Figure 1**a, only broad diffraction peaks could be observed in these XRD patterns, indicating the amorphous feature of the as-prepared borides. A further morphological investigation by the field-emission scanning electron microscopy (FESEM) suggested a similar morphology for all borides displaying nanoflowers assembled by the nanosheets (Figure 1b; Figures S1–S4, Supporting Information). Such a hierarchical nanoarchitecture is believed to be beneficial for the active site exposure and mass transfer during catalysis. To further corroborate the above observations, the microstructures of these compounds were examined by transmission electron microscopy (TEM) (Figure 1c–i, Figures S5–S8, Supporting Information). Taking NiB_2 as an example, the low-magnification TEM images for NiB_2 showed a similar morphology to that observed by FESEM (Figure 1c,d). Moreover, the high-resolution TEM (HRTEM) image demonstrated that there was no well-resolved lattice fringes (Figure 1e) and the corresponding selected area electron diffraction (SAED) pattern possessed halo rings (Figure 1f), both of which verified again the formation of amorphous structure, being well in agreement with the XRD observations. Furthermore, the energy-dispersive X-ray (EDX) element mapping (Figure 1g–i) revealed that Ni and B were homogeneously distributed within the architecture. Similar amorphous structure and nanosheet morphology of Ni_3B, Ni_2B, NiB, and NiB_3 was also found in their corresponding TEM results (Figures S5–S8, Supporting Information).

The composition and the valence states of elements in NiB_2 were analyzed by X-ray photoelectron spectroscopy (XPS). High-resolution XPS spectrum of Ni 2p (**Figure 2**a) confirmed the presence of Ni—B bonds (852.5 and 869.6 eV) in NiB_2 along with surface oxidized Ni^{2+} species (856.4 and 874.2 eV). Correspondingly, two peaks at 192.1 and 188.0 eV were observed in the B 1s spectrum (Figure S9, Supporting Information), which could be assigned to Ni—B bonds and surface passivated B^{3+}, respectively.[37–39] To further verify the chemical state of Ni and decouple the local structure, the NiB_2 was examined by both the X-ray absorption near-edge structure (XANES) spectroscopy and extended X-ray absorption fine structure (EXAFS) spectroscopy. It could be seen from the Ni K-edge XANES spectroscopy (Figure 2b) that the adsorption edge of NiB_2 was located between those of Ni foil and NiO references, indicating that the average valance state of Ni in NiB_2 was between metallic Ni^0 and oxidized Ni^{2+}, which was consistent with the XPS results. Moreover, the Ni K-edge EXAFS curves, as well as corresponding fitting results toward the Ni foil, NiO, and NiB_2,

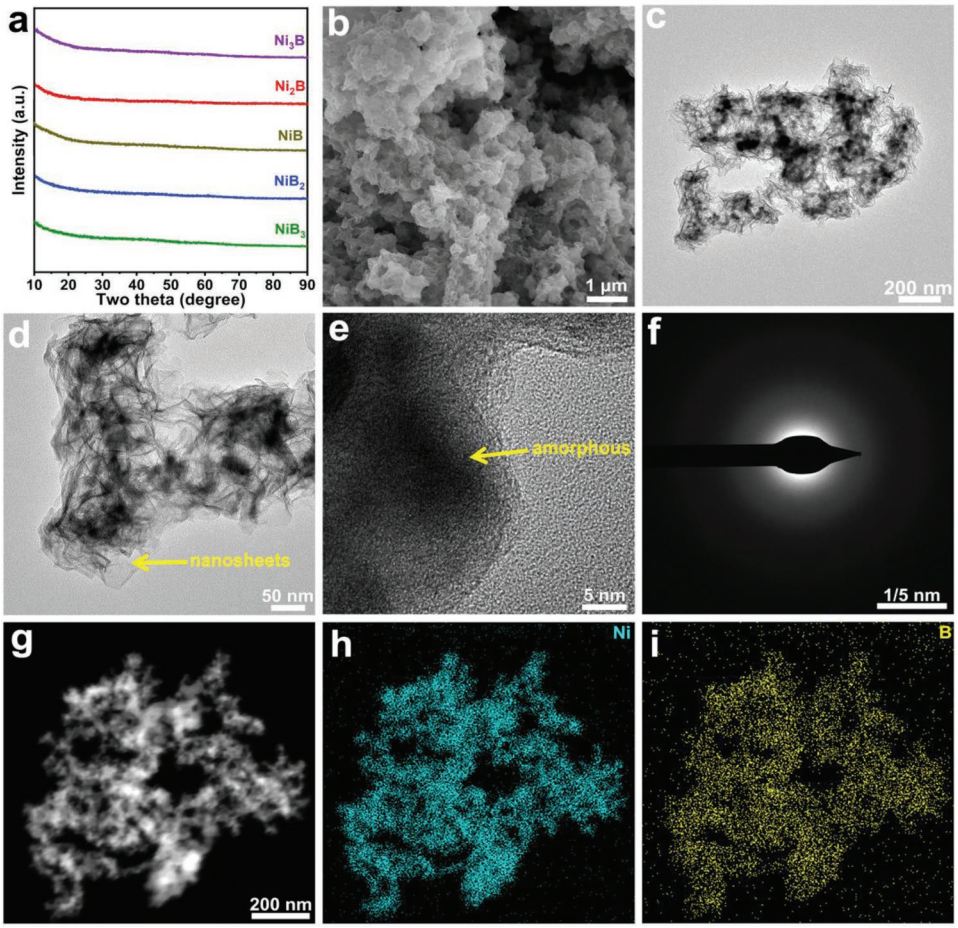

Figure 1. a) XRD patterns of a series of Ni–B compounds; b) FESEM image, c) low-magnification TEM image, d) middle-magnification TEM image, e) high-resolution TEM image, f) SAED pattern, g) HAADF image of representative NiB_2 and h,i) the corresponding elemental mappings of Ni (h) and B (i).

are also provided and compared (Figure 2c,d; Figures S10–S12, Supporting Information). Note that because the crystalline NiB_2 structure has not been previously reported, the structure model based on replacing Fe atoms by Ni atoms in the crystalline FeB_2 structure was selected for the EXAFS simulation trial.[40] Unexpectedly, the fitted *R* factor was quite good (0.0038), suggesting the rational and matched structure, that is, the local structure for amorphous NiB_2 alloy was similar to that for FeB_2. Specifically, it could be observed that NiB_2 displayed two main peaks at around 1.779 and 2.731 Å, respectively, accompanied by a submerged peak at around 2.110 Å, which were assigned to Ni–B coordination in the first shell, Ni–Ni coordination in the second shell and Ni–Ni coordination in the third shell, respectively. In order to further illustrate the coordination environment in NiB_2, wavelet transform (WT) was used to analyze the Ni K-edge EXAFS oscillations. The WT contour plots of Ni foil and NiO displayed the maximum intensity at 7.6 $Å^{-1}$ (Figure 2e) and 7.2 $Å^{-1}$ (Figure 2f), respectively, which could be due to their corresponding Ni–Ni coordination.[41,42] Compared to this, the maximum intensity was found to be positioned at 6.4 $Å^{-1}$ in the WT contour plot of NiB_2, which is ascribed to the coordination between Ni and B (Figure 2g).[43,44] According to the fitting results (Table S2, Supporting Information), unsaturated coordination numbers of B to Ni were observed in NiB_2, implying its defective structure, which might be beneficial to the ORR process.

Encouraged by the expected phase structure and micromorphology, the $2e^-$ ORR electrocatalytic activity of NiB_2 in 0.1 M O_2-saturated KOH was evaluated using a standard three-electrode system at room temperature, and compared with Ni_3B, Ni_2B, NiB, and NiB_3 phases. A rotating ring disk electrode (RRDE) was used to determine the selective oxygen reduction performance of the catalysts, and the collection efficiency was calculated as 0.37 (Figure S13, Supporting Information). The LSV curves of all five electrocatalysts toward ORR were compared and presented in **Figure 3**a. Evidently, NiB_2 exhibited a disk current close to the theoretical limit (3 mA cm^{-2}) of $2e^-$ ORR accompanied by a large and fast-rising ring current. The H_2O_2 selectivity and electron-transfer number were also extracted from the LSV curves. In a wide potential range, the H_2O_2 selectivity of the NiB_2 was calculated to be more than 93%, especially approaching 99% at 0.4 V vs RHE (Figure 3b), which was much higher than those of Ni_3B (60%), Ni_2B (82%), NiB (50%), and NiB_3 (35%). Analogously, the average electron-transfer number attained for NiB_2 was about 2.06, suggesting an almost complete $2e^-$ ORR process (Figure 3c). Besides, the

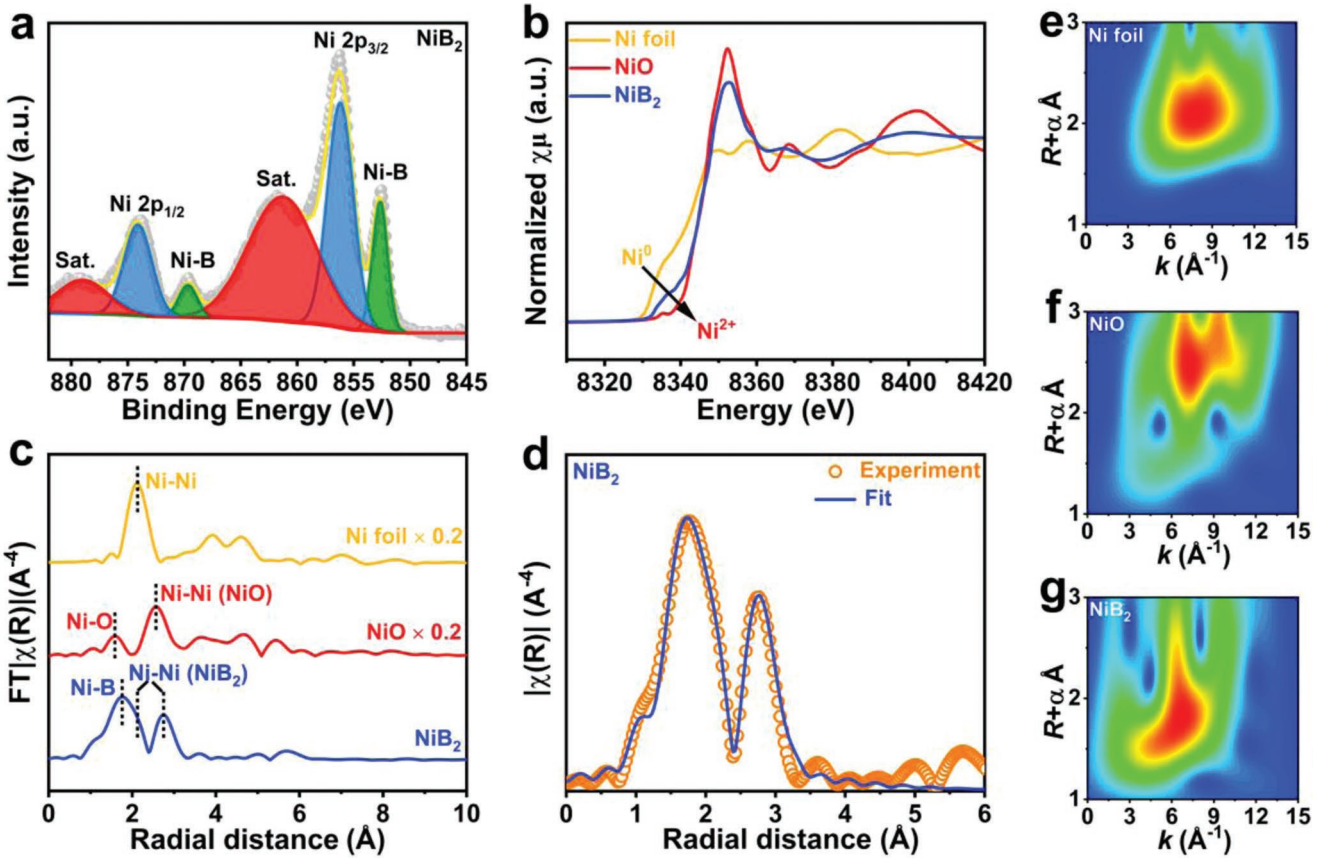

Figure 2. a) High-resolution XPS spectra of Ni 2p in NiB_2; b) normalized XANES spectra of Ni foil, NiO, and NiB_2 measured at the Ni K-edge; c) FT-EXAFS spectra of Ni foil, NiO, and NiB_2; d) FT-EXAFS fitting curve of NiB_2 in *R* space; e–g) wavelet transforms of Ni K-edge EXAFS data of Ni foil (e), NiO (f), and NiB_2 (g).

electron-transfer number during ORR for Ni_3B, Ni_2B, NiB, and NiB_3 was around 2.81, 2.33, 2.99, and 3.32, respectively, which were much higher than that of NiB_2, suggesting that $4e^-$ ORR was highly competitive during their ORR. These results also strongly demonstrated that the different atomic ratios between Ni and B played an important role in tuning the ORR pathway. Notably, the selectivity for amorphous NiB_2 toward $2e^-$ ORR ranked in the top level among the currently reported transition-metal-based electrocatalysts in a wide potential range from 0.2 to 0.6 V (Figure 3d; Table S3, Supporting Information). It should be remarked that the produced H_2O_2 might undergo further decomposition reaction in the presence of electrocatalysts. To check this, the H_2O_2 decomposition ability of the electrocatalysts was firstly estimated by the disproportionation reaction test. After adding 5 mg electrocatalysts into the 0.1 M KOH containing 10×10^{-3} M H_2O_2 solution, the results showed that NiB_2 exhibited a poor hydrogen peroxide disproportionation capability (Figure S14, Supporting Information). To further confirm this, the hydrogen peroxide reduction reaction measurement was then performed in Ar-saturated 0.1 M KOH containing 10×10^{-3} M H_2O_2. Even when the applied overpotential was increased, the H_2O_2 decomposition current density by NiB_2 was still minimal, showing excellent H_2O_2 retention ability, which was expected to be conducive to bulk H_2O_2 production (Figure S14, Supporting Information).

On the other hand, stability is an indispensable indicator to evaluate the ORR performance in practical applications. Bearing this point in mind, chronoamperometry was also employed to determine the long-term stability of NiB_2. The current of ring and disk electrodes was recorded in O_2-saturated 0.1 M KOH electrolyte, where the working electrode was fixed at 0.4 V vs RHE (Figure 3e). Both the i_{disk} and i_{ring} almost showed no current decay even after the 12 h test, ensuring superior performance compared to previously reported TM-based electrocatalysts (Table S3, Supporting Information). Notably, the H_2O_2 selectivity kept fluctuating at around 95% during the entire testing process. In addition, the accelerated degradation test (ADT) was carried out to examine the stability of the catalysts. As shown in Figure 3f, quite a little attenuation could be observed for NiB_2 even after 5000 (5 K) ADT cycles. Moreover, both the selectivity toward H_2O_2 (%) and electron transferred number for NiB_2 were well retained even after 5 K ADT cycles (Figure S15, Supporting Information), signifying the excellent catalytic stability of NiB_2.

To further understand the origin of the outstanding stability, the phase structure, morphology, and chemical state of the NiB_2 electrocatalyst after the durability test were comprehensively analyzed. The XRD pattern of NiB_2 after the ORR test was almost unchanged as compared to the as-prepared one (Figure S16a, Supporting Information), implying high

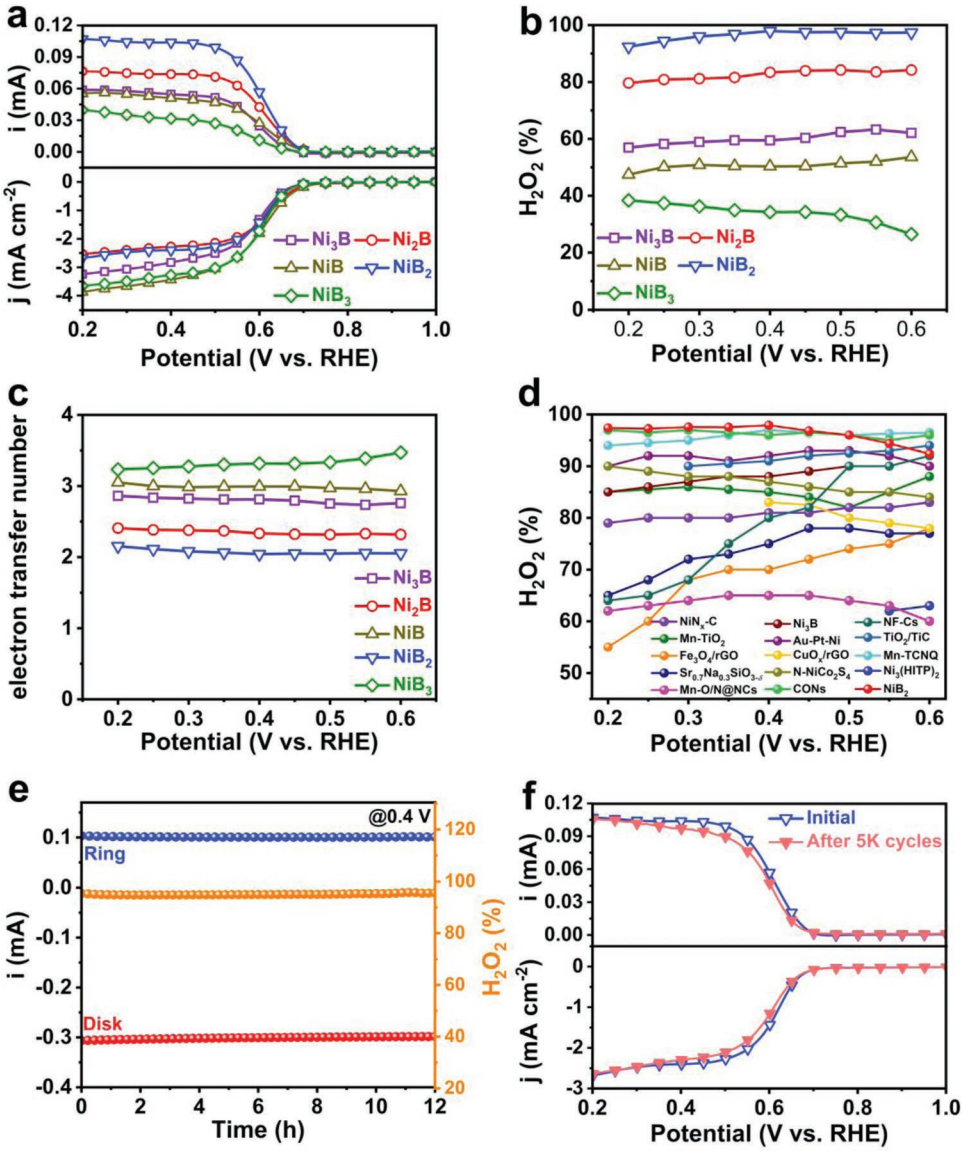

Figure 3. a) LSV curves of the five Ni–B samples, where the disk current density (j_{disk}) together with the ring currents (i_{ring}) was fixed at a potential of 1.50 V vs RHE. b) The calculated H_2O_2 (%) of the corresponding LSV curves. c) The calculated *n* of the corresponding LSV curves. d) Comparison of ORR selectivity of NiB_2 with previously reported electrocatalysts. e) Chronoamperometry of NiB_2 at 0.4 V vs RHE in O_2-saturated 0.1 M KOH for 12 h. f) Comparison of LSV curves of NiB_2 before and after 5 K ADT cycles.

structural stability. Similarly, the FESEM and TEM results also confirmed the high morphological stability (Figure S16b–i, Supporting Information), and the EDX results demonstrated that the elemental composition was preserved against ORR cycling (Table S4, Supporting Information). Furthermore, XPS was conducted to acquire the surface information of the NiB_2 after the chronoamperometry test (Figure S17, Supporting Information). The high-resolution XPS spectrum of Ni 2p was quite similar to the fresh NiB_2, suggesting a marginal surface reconstruction, which could be commonly observed in previous reports and believed to improve the oxygen adsorption ability to promote the $2e^-$ ORR process.[45–47]

Inspired by the outstanding $2e^-$ ORR activity, selectivity and stability, the H_2O_2 production ability on a large scale was verified for NiB_2. First, an H-type electrolytic cell was employed to determine the H_2O_2 yield (Figure S18, Supporting Information). The H_2O_2 yield was measured in an O_2-saturated 0.1 M KOH electrolyte with an applied potential of 0.4 V vs RHE. Remarkably, the H_2O_2 yield was determined as 1.079 mol g^{-1}_{cat} h^{-1} by the UV–vis spectrum (Figure S19, Supporting Information). Given the fact that the production rate of H_2O_2 in the H-type electrolytic cell was restricted by the limitation of oxygen diffusion capability, the gas diffusion electrode was assembled to address this issue (**Figure 4**a; Figure S20, Supporting Information). As expected, the diffusion capability of oxygen to active sites was greatly improved, hence a larger oxygen reduction current and a higher H_2O_2 yield were achieved. The comparison of LSV curves recorded in O_2 and

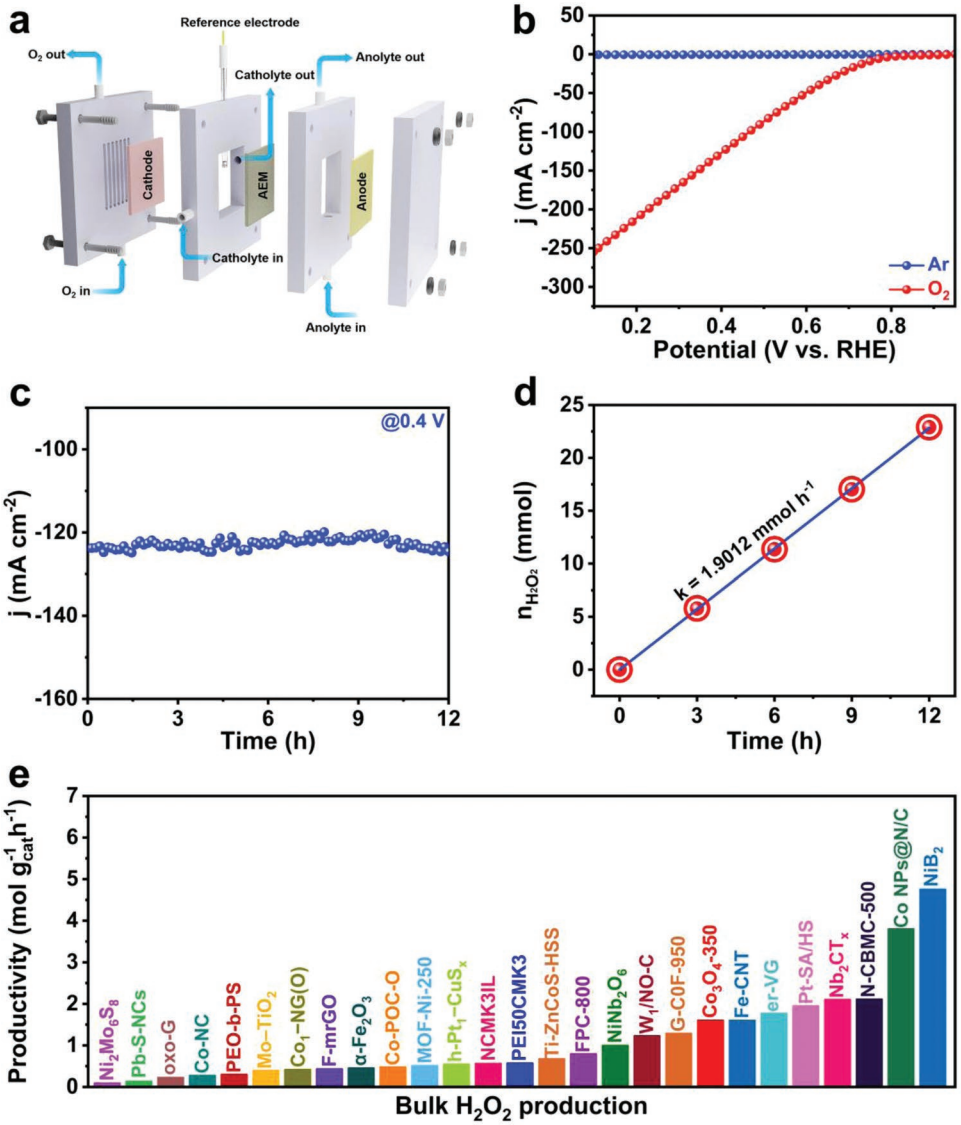

Figure 4. a) Schematic diagram of the gas diffusion electrode used for H_2O_2 electrochemical synthesis. b) Linear sweep voltammetry of gas diffusion electrode under O_2 and Ar. c) Chronoamperometric curve under the O_2 condition of gas diffusion electrode. d) Moles of H_2O_2 generated by NiB_2 as a function of electrolysis time under the condition of continuous O_2 in the gas diffusion electrode. e) Comparison of bulk H_2O_2 production of NiB_2 with previously reported electrocatalysts.

Ar-saturated 0.1 M KOH electrolyte strongly suggested the oxygen reduction ability of NiB_2 (Figure 4b). Moreover, high current densities were observed with the assistance of gas diffusion electrodes, indicating the potential of H_2O_2 production on a large scale. When the potential applied to the working electrode was 0.4 V vs RHE, a current density of 125 mA cm^{-2} was achieved by the gas diffusion electrode (Figure 4c). The H_2O_2 yield was determined up to around 1.9012 mmol h^{-1} and 4.753 mol g^{-1}_{cat} h^{-1}, which was greatly exceeded the value in the H-type electrolytic cell (Figure 4d). Moreover, NiB_2 delivered a Faradaic efficiency of 93%, which was close to the theoretical one. The reasons for less than 100% efficiency could be ascribed to the decomposition of H_2O_2 under alkaline conditions and/or the occurrence of $4e^-$ ORR on carbon paper. The exceptional durability of continuous operation of NiB_2 in gas diffusion electrodes further demonstrated the potential in practical application. Even after a continuous 12 h testing, the current density of the gas diffusion electrode was still well maintained at about 125 mA cm^{-2}, and little activity decay was observed (Figure 4c,d). Moreover, this H_2O_2 productivity and continuous H_2O_2 production capacity surpassed nearly all recently reported $2e^-$ ORR TM-based electrocatalysts (Figure 4e and Table S5, Supporting Information). It has been well documented that amorphous materials bear a higher density of surface defects (e.g., high density of coordinatively unsaturated sites) than their crystalline counterparts, which can usually enhance the electrocatalytic activities.[48–50] Specifically, the presence of abundant defects not only contributes to the exposure of active metal sites, which increases the amount of catalytic sites during catalysis but also modifies the charge distribution of

active metal sites, thus altering the charge-transfer ability and free adsorption energy toward surface-bound intermediates. To confirm this, the double-layer capacitance (C_{dl}) that was positively correlated to electrochemical active surface area (ECSA), electrochemical impedance spectroscopy (EIS), XPS spectra and ORR activity of amorphous N_3B and crystalline Ni_3B alloys were compared under the same testing condition as an illustration (Figures S21–S25, Supporting Information). Note that crystalline NiB_2 was not selected because of the fact that it was hard to be achieved due to the high tendency to undergo the disproportionation-like reaction for amorphous NiB_2 during annealing (Figure S26, Supporting Information). The amorphous N_3B showed a much higher C_{dl} value (6.540 mF cm^{-2}) than that of the crystalline counterpart (1.080 mF cm^{-2}), demonstrating the larger amount of potential active sites (Figure S21, Supporting Information). Moreover, a slightly higher charge-transfer resistance was observed for amorphous Ni_3B than crystalline Ni_3B during catalysis, meaning the relatively slow charge-transfer kinetics (Figure S22, Supporting Information), which was probably beneficial for suppressing 4e⁻ ORR. Furthermore, the XPS spectra showed a slight change in both Ni and B valance states between crystalline Ni_3B and amorphous Ni_3B, implying the change in the electronic structure of Ni_3B (Figure S23, Supporting Information). Such a variation of the electronic structure in amorphous architecture probably effectively optimized the adsorption free energy of metal sites toward *OOH for improving 2e⁻ ORR.[17,51] As a result, benefiting from the above merits, the amorphous Ni_3B delivered about 10% selectivity higher than that of the corresponding crystalline one (Figure S24, Supporting Information). The ORR performance of the annealed NiB_2 sample was also compared to the amorphous one under the same condition and lower activity and selectivity toward 2e⁻ ORR for the annealed sample was attained (Figure S25, Supporting Information), demonstrating again the advantages of amorphous structure. On the other hand, the C_{dl} value for five amorphous nickel borides was also compared. From the results, it could be seen that with the increase of metal amount in borides, the C_{dl} value was gradually increased, meaning the increase in the amount of catalytically active sites (Figure S27, Supporting Information).

To unveil the origin of the superior activity of NiB_2 toward 2e⁻ ORR, the in situ Raman test was performed in 0.1 M KOH (0.3–0.7 V vs RHE) to gather insights into the possible active sites. As shown in **Figure 5**a, the bottom Raman curve was recorded at 0.7 V vs RHE, which is close to the onset potential and no obvious peaks can be observed. Moreover, the signals at 178, 435, and 731 cm^{-1} were gradually augmented as the ORR underwent (0.05 V as an interval), which can be attributed to the Ni–O signals.[52–54] Therefore, the reaction mainly occurred on Ni sites. Based on the in situ Raman test result, the density functional theoretical (DFT) calculation was carried out by taking the Ni site as the active site. Since the amorphous structure presented the short order arrangement feature, cluster models for amorphous Ni_3B, Ni_2B, NiB, NiB_2, and NiB_3 phases were rationally created. Then, the free adsorption energy toward the intermediate *OOH (ΔG_{OOH*}) was calculated and depicted in Figure 5b. Within different borides, NiB_2 showed the closest ΔG_{OOH*} value (3.75 eV) to the ideal value of 3.52 eV suggesting the best balance of adsorption and desorption ability toward *OOH,[9,21,55,56] which was in favor of the preservation of O—O bond and production of H_2O_2. The limiting potential–volcano plot for the 2e⁻ ORR pathway by using ΔG_{OOH*} as a descriptor was further depicted. NiB_2 cluster showed the nearest position to the top site of the volcano plot among the nickel boride samples, suggesting the most active H_2O_2 production (Figure S28, Supporting Information). Such activity also surpassed some previously reported representative 2e⁻ ORR electrocatalysts and was also comparable to the noble metal ones.[3,11,30,55,57] To further demonstrate the high 2e⁻ ORR selectivity, we have provided the energy diagram for the reaction pathway of 4e⁻ ORR for NiB_2 electrocatalyst for comparison. The free adsorption energy barrier was about +0.21 V for the conversion of *OOH to *O, which was larger than that (–0.23 eV) of the conversion of *OOH to *O under 0.7 V vs RHE, demonstrating the high two-electron selectivity (Figure S29, Supporting Information). Furthermore, when the ratio of Ni to B was high, such as for Ni_3B, Ni_2B, and NiB, the adsorption model for *OOH presented in the form of a side-on model (Figure 5c–e), which was believed to be hard for the preservation of O—O bond. However, when the ratio of B to Ni was high, the B atoms could effectively be served as the fence to isolate neighboring Ni atoms, which led to the end-on adsorption model of *OOH and facilitated the preservation of O—O bond (Figure 5f,g). Note that according to the deviation degree of ΔG_{OOH*} value to 3.52 eV, it could be concluded that the activity showed the enhancement in the tendency of $NiB_2 > Ni_2B > NiB_3 > Ni_3B > NiB$. This tendency was slightly different from the experimental observations ($NiB_2 > Ni_2B > Ni_3B > NiB > NiB_3$), which could be due to the comprehensive impact of the free adsorption energy toward *OOH, interfacial charge-transfer ability as well as the amount of active Ni sites as discussed below. Differential charge density distribution between the substrate and *OOH was decoupled and provided in Figure 5c–g. By comparing these patterns, the charge polarization occurred for all OOH-adsorbed cluster models. Among them, NiB_3 showed a relatively weak charge interaction between *OOH and substrate, while Ni_2B, Ni_3B, and NiB showed a strong one. In comparison with these, NiB_2 displayed a modest charge interaction between the substrate and *OOH resulting in an enhancement of catalytic activity. Notably, these results indicated that the electronic structure and adsorption model could be tuned by the atomic ratio between Ni and B, and thereby an optimization of ΔG_{OOH*}. Motivated by the outstanding 2e⁻ ORR activity and selectivity in alkaline media, the 2e⁻ ORR performance for NiB_2 was further investigated in 0.05 M H_2SO_4. Unfortunately, NiB_2 delivered activity with a larger overpotential and a lower H_2O_2 selectivity as compared to that under alkaline media (Figure S30, Supporting Information). The energy diagram for the reaction pathway from O_2 to H_2O_2 in the acidic solution was also calculated by DFT. The energy diagram showed that NiB_2 bears a larger deviation of ΔG_{OOH*} to 3.52 eV ($U = 0.7$ V) under acidic media than under alkaline media (Figure S31, Supporting Information).

In addition to DFT, the interfacial electron transfer process was analyzed to figure out the effect of electronic structure on ORR performance. A stimulation-response technique was developed based on a transient photoinduced voltage (TPV) to record the electron transfer process.[58–60] The TPV curves of Ni_3B and Ni_2B were first plotted in **Figure 6**a, from which

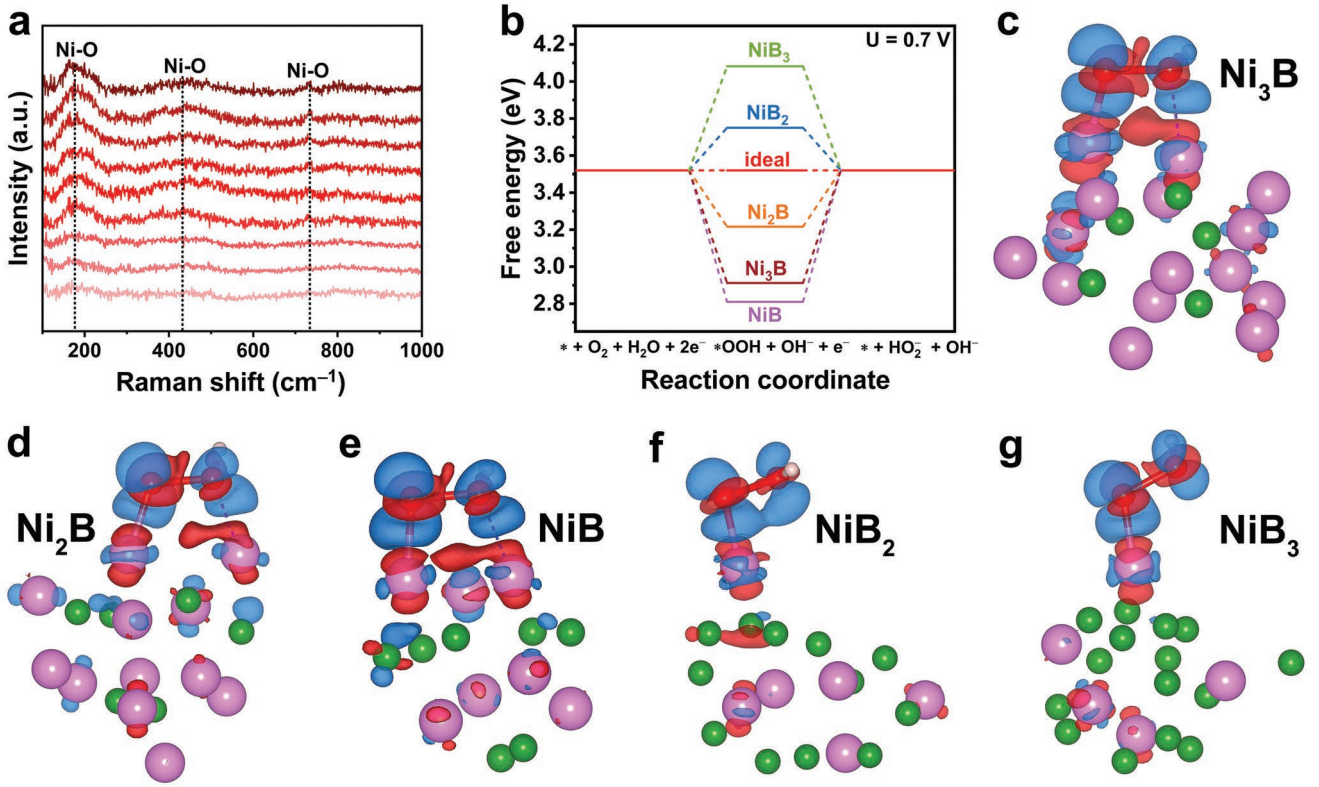

Figure 5. a) In situ Raman spectra for NiB_2 electrocatalyst in O_2-saturated 0.1 M KOH within voltage window 0.3–0.7 V vs RHE. b) Free energy diagram at the limiting potential $U = 0.7$ V for nickel boride clusters with a different atomic ratio between Ni and B. c–g) Differential charge density distribution between *OOH with Ni_3B (c), Ni_2B (d), NiB (e), NiB_2 (f), and NiB_3 (g) substrate. (The atoms in pink, green, red, and light pink represent Ni, B, O, and H, respectively; the red and blue colored isosurfaces mean the positive charge and the negative charge, respectively.)

it could be observed that these two curves show similar decay tendency, that is, the intensity decreased with prolonged time. The decay time of Ni_3B and Ni_2B was simulated as 0.3299 and 0.3877 ms, respectively, meaning that the overall electron transfer process on the surface of Ni_2B was slower than that of Ni_3B. In general, the slower electron transfer kinetics would render the accumulation of electrons at the surface for a longer time rather than being quickly transformed into O_2 molecules, which could enhance the $2e^-$ ORR activity.[61,62] Interestingly, NiB, NiB_2, and NiB_3 showed completely different curves where the signal intensity of the curves decayed even less than zero as time proceeded, which could be due to the electron-trap effect (Figure 6b). The emergence of the electron-trap effect usually signifies that the sample bears a strong ability to capture interfacial electrons and leads to slower electron transfer on the surface of the catalyst, thus facilitating the $2e^-$ ORR. Moreover, the decay times of the NiB, NiB_2, and NiB_3 were also simulated as 0.1526, 0.3032, and 0.2135 ms, respectively.

In order to deeply decouple the electron transfer on the surface of the electrocatalysts, fast Fourier transform (FFT) was adopted based on the TPV data. The FFT curves of the five electrocatalysts are displayed in Figure 6c, which showed a series of continuous signals. No obvious peaks were found in these FFT curves, revealing that there was no apparent static and periodic frequency component presented in the TPV relaxation signals. The continuous wavelet transformation (CWT) curves were also displayed to reveal different decay processes. Therefore, the CWT pattern of Ni_3B and Ni_2B were provided (Figure 6d and Figure S32, Supporting Information). The obtained CWT patterns were presented in the form 3D diagram, involving the time, frequency, and intensity, which provided time-scale/frequency-scale analysis of these TPV curves. For different TPV curves, the relationship between peak intensity and time at different frequencies was compared to elucidate the dynamic electron transfer process, in which the low and high frequency represents slow and fast electron transfer, respectively. As shown in Figure 6e, the peak positions of Ni_3B and Ni_2B at 15 Hz were 0.6105 (t_1) and 0.6335 ms (t_2), respectively, which suggested that Ni_2B displayed a relatively slow interfacial electron transfer process in the low-frequency region. Moreover, even when the frequency was increased to 20 Hz, which corresponded to a faster interfacial electron transfer than 15 Hz, the position (0.4865 ms, t_2) of the peak observed in Ni_2B was still smaller than that (0.4725 ms, t_1) of Ni_3B (Figure 6f). The comparison of peak positions at other frequencies also showed that Ni_2B displayed lagging peaks as compared to those of Ni_3B (Figure S33, Supporting Information). The time difference ($\Delta t_{2-1} = t_2 - t_1$) at the fixed frequency was further achieved to investigate the difference in the different interfacial transport processes in which the Δt were 0.0230 ms at 15 Hz and 0.0140 ms at 20 Hz. For some other higher frequencies, the Δt was very close to zero (Table S6, Supporting Information). On the whole, the

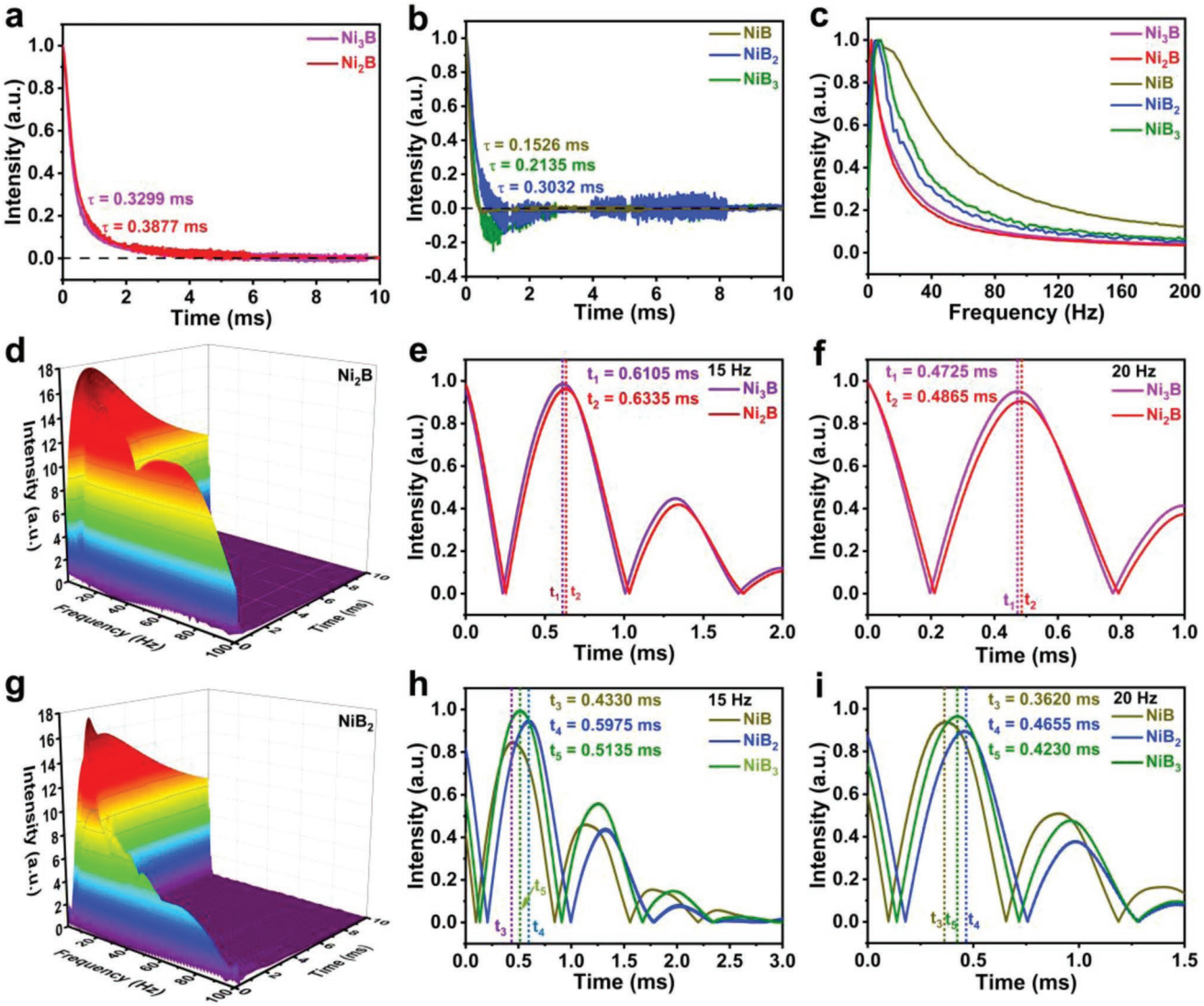

Figure 6. a) TPV curves and corresponding decay times of Ni_3B and Ni_2B. b) TPV curves and corresponding decay times of NiB, NiB_2, and NiB_3. c) FFT patterns of the five TPV curves. d) CWT pattern of the corresponding Ni_2B TPV curve. e,f) Intensity–time curves comparison of Ni_3B and Ni_2B (t_1 and t_2 are the peak occurrence time of Ni_3B and Ni_2B, respectively). g) CWT pattern of the corresponding NiB_2 TPV curve. h,i) Intensity–time curves comparison of NiB, NiB_2, and NiB_3 (t_3, t_4, and t_5 are the peak occurrence time of NiB, NiB_2, and NiB_3, respectively).

Δt_{2-1} became minimal as the frequencies increased. It means that the most significant distinction in electron transfer was at low frequencies, and Ni_2B displayed a slower interfacial transport process than that of Ni_3B, which was beneficial to the $2e^-$ ORR and resulted in a higher H_2O_2 selectivity.

Next, the interfacial electron transfer for NiB, NiB_2, and NiB_3 electrocatalysts were also compared. At 15 Hz (Figure 6h), NiB_2 presented a lagging peak (t_4 = 0.5975 ms) than those of NiB (t_3 = 0.4330 ms) and NiB_3 (t_5 = 0.5135 ms), indicating that NiB_2 exhibited the slowest interfacial electron transfer in low frequency region. As shown in Figure 6i, three samples presented obvious peak positions at 20 Hz, they were t_3 = 0.362 ms for NiB, t_4 = 0.465 ms for NiB_2 and t_5 = 0.424 ms for NiB_3, respectively. NiB_2 also showed a hysteretic peak position than those of NiB and NiB_3, and NiB_3 displayed apparently lagging compared with that of NiB. Similarly, at other frequencies, the electron transfer kinetics still showed the enhanced tendency in the order of NiB_2 < NiB_3 < NiB (Figure S34, Supporting Information). Moreover, the time differences ($\Delta t_{4-5} = t_4 - t_5$ and $\Delta t_{5-3} = t_5 - t_3$) were also achieved to illustrate the decisive frequency range that caused the electron transfer difference among the three electrocatalysts (Tables S7 and S8, Supporting Information). These results clearly indicated that the main difference in electron transfer occurred in the low-frequency region. This hysteresis may be beneficial in $2e^-$ ORR, as it caused electrons at the catalyst interface to stay at the interface for a longer period of time instead of being transferred to O_2 molecules. Therefore, NiB_2 possessed the slowest interfacial charge transfer kinetics among all the electrocatalysts, which would be the most effective to inhibit the binding of adjacent *OOH to form O_2. The above results show that NiB_2 has a favorable binding strength for OOH* and the

slowest interfacial electron transfer kinetics, which synergistically assured the best activity and selectivity.

3. Conclusion

Several amorphous nickel borides nanosheets with different electronic structures were achieved by altering the composition ratio between Ni and B. The activity investigations showed that the optimized NiB_2 was an efficient electrocatalyst for the electrochemical reduction of O_2 to H_2O_2, which delivered the highest selectivity of close to 99% at 0.4 V vs RHE and produced over 93% of selectivity of H_2O_2 across a wide potential range from 0.2 to 0.6 V vs RHE. Remarkably, the activity is stable with negligible current loss even after 12 h duration at 0.4 V vs RHE. Impressively, the sustainable bulk H_2O_2 productivity in the rate of up to 4.753 mol g_{cat}^{-1} h^{-1} can be stably recorded for at least 12 h by assembling the gas diffusion electrode, together with a high FE of around 93%, which are superior to nearly all previously reported TM-based electrocatalysts, showing huge potential for practical application. Further in situ and ex situ investigations combined with the computational analysis unveiled that the electronic structure for the amorphous NiB_2 phase not only bears the closest ΔG_{OOH*} value to the ideal one but also reduced electron-transfer capability on the surface, thus enhancing the catalytic activity and selectivity for the efficient production of H_2O_2. The discovery of this work not only renders the amorphous NiB_2 as a new representative benchmark for $2e^-$ ORR electrocatalyst in alkaline solution but also provides new mechanistic insights and opens up a new rational design strategy for economical, stable, and efficient TM electrocatalysts.

Supporting Information

Supporting Information is available from the Wiley Online Library or from the author.

Acknowledgements

J.W. and M.H. contributed equally to this work. This work was supported by National MCF Energy R&D Program of China (2018YFE0306105), National Key R&D Program of China (2020YFA0406104, 2020YFA0406101), Innovative Research Group Project of the National Natural Science Foundation of China (51821002), National Natural Science Foundation of China (51725204, 21771132, 51972216, 52041202), Natural Science Foundation of Jiangsu Province (BK20210735), Natural Science Foundation of the Higher Education Institutions of Jiangsu Province (21KJB430043), Collaborative Innovation Center of Suzhou Nano Science & Technology, the 111 Project, and Suzhou Key Laboratory of Functional Nano & Soft Materials. Z.C. gratefully acknowledges the funding from Alexander von Humboldt (AvH) Foundation. H.Y. thanks China Scholarship Council (CSC) for the Ph.D. fellowship. P.W.M. greatly acknowledges support from the German Federal Ministry of Education and Research in the framework of the project Catlab (03EW0015A/B).

Open access funding enabled and organized by Projekt DEAL.

Conflict of Interest

The authors declare no conflict of interest.

Data Availability Statement

The data that support the findings of this study are available from the corresponding author upon reasonable request.

Keywords

amorphous phase, charge transfer, electronic structure, hydrogen peroxide, oxygen reduction reaction

Received: April 1, 2022
Revised: May 18, 2022
Published online: July 12, 2022

[1] C. Xia, Y. Xia, P. Zhu, L. Fan, H. Wang, *Science* **2019**, *366*, 226.
[2] M. Melchionna, P. Fornasiero, M. Prato, *Adv. Mater.* **2019**, *31*, 1802920.
[3] E. Jung, H. Shin, B. H. Lee, V. Efremov, S. Lee, H. S. Lee, J. Kim, W. Hooch Antink, S. Park, K. S. Lee, S. P. Cho, J. S. Yoo, Y. E. Sung, T. Hyeon, *Nat. Mater.* **2020**, *19*, 436.
[4] T. Ricciardulli, S. Gorthy, J. S. Adams, C. Thompson, A. M. Karim, M. Neurock, D. W. Flaherty, *J. Am. Chem. Soc.* **2021**, *143*, 5445.
[5] E. Jung, H. Shin, W. Hooch Antink, Y.-E. Sung, T. Hyeon, *ACS Energy Lett.* **2020**, *5*, 1881.
[6] L. Yang, J. Shui, L. Du, Y. Shao, J. Liu, L. Dai, Z. Hu, *Adv. Mater.* **2019**, *31*, 1804799.
[7] C. Krishnaraj, H. Sekhar Jena, L. Bourda, A. Laemont, P. Pachfule, J. Roeser, C. V. Chandran, S. Borgmans, S. M. J. Rogge, K. Leus, C. V. Stevens, J. A. Martens, V. Van Speybroeck, E. Breynaert, A. Thomas, P. Van Der Voort, *J. Am. Chem. Soc.* **2020**, *142*, 20107.
[8] Y. Sun, L. Han, P. Strasser, *Chem. Soc. Rev.* **2020**, *49*, 6605.
[9] S. Siahrostami, S. J. Villegas, A. H. Bagherzadeh Mostaghimi, S. Back, A. B. Farimani, H. Wang, K. A. Persson, J. Montoya, *ACS Catal.* **2020**, *10*, 7495.
[10] D. Iglesias, A. Giuliani, M. Melchionna, S. Marchesan, A. Criado, L. Nasi, M. Bevilacqua, C. Tavagnacco, F. Vizza, M. Prato, P. Fornasiero, *Chem* **2018**, *4*, 106.
[11] X. Li, S. Tang, S. Dou, H. J. Fan, T. S. Choksi, X. Wang, *Adv. Mater.* **2022**, *34*, 2104891.
[12] P. T. Smith, Y. Kim, B. P. Benke, K. Kim, C. J. Chang, *Angew. Chem., Int. Ed.* **2020**, *59*, 4902.
[13] S. Back, J. Na, Z. W. Ulissi, *ACS Catal.* **2021**, *11*, 2483.
[14] J. Y. Zhang, C. Xia, H. F. Wang, C. Tang, *J. Energy Chem.* **2022**, *67*, 432.
[15] C. Liu, H. Li, J. Chen, Z. Yu, Q. Ru, S. Li, G. Henkelman, L. Wei, Y. Chen, *Small* **2021**, *17*, 2007249.
[16] H. Zhao, Z. Y. Yuan, *ChemSusChem* **2021**, *14*, 1616.
[17] Q. Chen, C. Ma, S. Yan, J. Liang, K. Dong, Y. Luo, Q. Liu, T. Li, Y. Wang, L. Yue, B. Zheng, Y. Liu, S. Gao, Z. Jiang, W. Li, X. Sun, *ACS Appl. Mater. Interfaces* **2021**, *13*, 46659.
[18] Q. Yuan, J. Zhao, D. H. Mok, Z. Zheng, Y. Ye, C. Liang, L. Zhou, S. Back, K. Jiang, *Nano Lett.* **2022**, *22*, 1257.
[19] H. Sheng, E. D. Hermes, X. Yang, D. Ying, A. N. Janes, W. Li, J. R. Schmidt, S. Jin, *ACS Catal.* **2019**, *9*, 8433.
[20] H. Sheng, A. N. Janes, R. D. Ross, D. Kaiman, J. Huang, B. Song, J. R. Schmidt, S. Jin, *Energy Environ. Sci.* **2020**, *13*, 4189.
[21] Z. Zhou, Y. Kong, H. Tan, Q. Huang, C. Wang, Z. Pei, H. Wang, Y. Liu, Y. Wang, S. Li, X. Liao, W. Yan, S. Zhao, *Adv. Mater.* **2022**, *34*, 2106541.
[22] H. Kim, J. Lim, S. Lee, H. H. Kim, C. Lee, J. Lee, W. Choi, *Environ. Sci. Technol.* **2019**, *53*, 2918.
[23] F. Razmjooei, C. Pak, J.-S. Yu, *ChemElectroChem* **2018**, *5*, 1985.

[24] Z. Chen, J. Wu, Z. Chen, H. Yang, K. Zou, X. Zhao, R. Liang, X. Dong, Z. Kang, P. W. Menezes, *Angew. Chem., Int. Ed.* **2022**, *61*, e202200086.
[25] H. Huang, A. Cho, S. Kim, H. Jun, A. Lee, J. W. Han, J. Lee, *Adv. Funct. Mater.* **2020**, *30*, 2003889.
[26] G. Kwon, H. Jang, J. S. Lee, A. Mane, D. J. Mandia, S. R. Soltau, L. M. Utschig, A. B. F. Martinson, D. M. Tiede, H. Kim, J. Kim, *J. Am. Chem. Soc.* **2018**, *140*, 10710.
[27] Z. Xu, J. Liang, Y. Wang, K. Dong, X. Shi, Q. Liu, Y. Luo, T. Li, Y. Jia, A. M. Asiri, Z. Feng, Y. Wang, D. Ma, X. Sun, *ACS Appl. Mater. Interfaces* **2021**, *13*, 33182.
[28] H. Han, H. Choi, S. Mhin, Y.-R. Hong, K. M. Kim, J. Kwon, G. Ali, K. Y. Chung, M. Je, H. N. Umh, D.-H. Lim, K. Davey, S.-Z. Qiao, U. Paik, T. Song, *Energy Environ. Sci.* **2019**, *12*, 2443.
[29] W. Hao, D. Yao, Q. Xu, R. Wang, C. Zhang, Y. Guo, R. Sun, M. Huang, Z. Chen, *Appl. Catal., B* **2021**, *292*, 120188.
[30] F. Ma, S. Wang, X. Liang, C. Wang, F. Tong, Z. Wang, P. Wang, Y. Liu, Y. Dai, Z. Zheng, B. Huang, *Appl. Catal. B* **2020**, *279*, 119371.
[31] W. Lu, T. Liu, L. Xie, C. Tang, D. Liu, S. Hao, F. Qu, G. Du, Y. Ma, A. M. Asiri, X. Sun, *Small* **2017**, *13*, 1700805.
[32] Z. Chen, H. Yang, Z. Kang, M. Driess, P. W. Menezes, *Adv. Mater.* **2022**, *34*, 2108432.
[33] Y. Kang, B. Jiang, J. Yang, Z. Wan, J. Na, Q. Li, H. Li, J. Henzie, Y. Sakka, Y. Yamauchi, T. Asahi, *ACS Nano* **2020**, *14*, 17224.
[34] B. Jiang, H. Song, Y. Kang, S. Wang, Q. Wang, X. Zhou, K. Kani, Y. Guo, J. Ye, H. Li, Y. Sakka, J. Henzie, Y. Yusuke, *Chem. Sci.* **2019**, *11*, 791.
[35] Y. Kang, J. Henzie, H. Gu, J. Na, A. Fatehmulla, B. S. A. Shamsan, A. M. Aldhafiri, W. A. Farooq, Y. Bando, T. Asahi, B. Jiang, H. Li, Y. Yamauchi, *Small* **2020**, *16*, 1906707.
[36] Y. Kang, B. Jiang, V. Malgras, Y. Guo, O. Cretu, K. Kimoto, A. Ashok, Z. Wan, H. Li, Y. Sugahara, Y. Yamauchi, T. Asahi, *Small Methods* **2021**, *5*, 2100679.
[37] S. Barwe, J. Weidner, S. Cychy, D. M. Morales, S. Dieckhofer, D. Hiltrop, J. Masa, M. Muhler, W. Schuhmann, *Angew. Chem., Int. Ed.* **2018**, *57*, 11460.
[38] M. Lewandowski, *Appl. Catal. B* **2015**, *168*, 322.
[39] M. Arif, G. Yasin, M. Shakeel, M. A. Mushtaq, W. Ye, X. Fang, S. Ji, D. Yan, *J. Energy Chem.* **2021**, *58*, 237.
[40] H. Li, P. Wen, Q. Li, C. Dun, J. Xing, C. Lu, S. Adhikari, L. Jiang, D. L. Carroll, S. M. Geyer, *Adv. Energy Mater.* **2017**, *7*, 1700513.
[41] J. Pan, G. Zhang, Z. Guan, Q. Zhao, G. Li, J. Yang, Q. Li, Z. Zou, *J. Energy Chem.* **2021**, *58*, 408.
[42] S. Jin, Y. Ni, Z. Hao, K. Zhang, Y. Lu, Z. Yan, Y. Wei, Y. R. Lu, T. S. Chan, J. Chen, *Angew. Chem., Int. Ed.* **2020**, *59*, 21885.
[43] J. Masa, I. Sinev, H. Mistry, E. Ventosa, M. de la Mata, J. Arbiol, M. Muhler, B. R. Cuenya, W. Schuhmann, *Adv. Energy Mater.* **2017**, *7*, 1700381.
[44] Y. R. Hong, K. M. Kim, J. H. Ryu, S. Mhin, J. Kim, G. Ali, K. Y. Chung, S. Kang, H. Han, *Adv. Funct. Mater.* **2020**, *30*, 2004330.
[45] M. Wang, N. Zhang, Y. Feng, Z. Hu, Q. Shao, X. Huang, *Angew. Chem., Int. Ed.* **2020**, *59*, 14373.
[46] X. Han, W. Zhang, X. Ma, C. Zhong, N. Zhao, W. Hu, Y. Deng, *Adv. Mater.* **2019**, *31*, 1808281.
[47] F. Xia, B. Li, Y. Liu, Y. Liu, S. Gao, K. Lu, J. Kaelin, R. Wang, T. J. Marks, Y. Cheng, *Adv. Funct. Mater.* **2021**, *31*, 2104716.
[48] A. M. Alexander, J. S. Hargreaves, *Chem. Soc. Rev.* **2010**, *39*, 4388.
[49] S. Anantharaj, S. Noda, *Small* **2020**, *16*, 1905779.
[50] S. Gupta, M. K. Patel, A. Miotello, N. Patel, *Adv. Funct. Mater.* **2019**, *30*, 1906481.
[51] Z. Wu, T. Wang, J.-J. Zou, Y. Li, C. Zhang, *ACS Catal.* **2022**, *12*, 5911.
[52] M. W. Louie, A. T. Bell, *J. Am. Chem. Soc.* **2013**, *135*, 12329.
[53] N. Kurra, N. A. Alhebshi, H. N. Alshareef, *Adv. Energy Mater.* **2015**, *5*, 1401303.
[54] Z. Qiu, C.-W. Tai, G. A. Niklasson, T. Edvinsson, *Energy Environ. Sci.* **2019**, *12*, 572.
[55] S. Siahrostami, A. Verdaguer-Casadevall, M. Karamad, D. Deiana, P. Malacrida, B. Wickman, M. Escudero-Escribano, E. A. Paoli, R. Frydendal, T. W. Hansen, I. Chorkendorff, I. E. Stephens, J. Rossmeisl, *Nat. Mater.* **2013**, *12*, 1137.
[56] J. Gao, H. b. Yang, X. Huang, S.-F. Hung, W. Cai, C. Jia, S. Miao, H. M. Chen, X. Yang, Y. Huang, T. Zhang, B. Liu, *Chem* **2020**, *6*, 658.
[57] H. Zhao, X. Shen, Y. Chen, S. N. Zhang, P. Gao, X. Zhen, X. H. Li, G. Zhao, *Chem. Commun.* **2019**, *55*, 6173.
[58] Q. Wu, J. Cao, X. Wang, Y. Liu, Y. Zhao, H. Wang, Y. Liu, H. Huang, F. Liao, M. Shao, Z. Kang, *Nat. Commun.* **2021**, *12*, 483.
[59] J. Wu, Y. Zhou, H. Nie, K. Wei, H. Huang, F. Liao, Y. Liu, M. Shao, Z. Kang, *J. Energy Chem.* **2022**, *66*, 61.
[60] Y. Zhao, L. Xu, X. Wang, Z. Wang, Y. Liu, Y. Wang, Q. Wang, Z. Wang, H. Huang, Y. Liu, W.-Y. Wong, Z. Kang, *Nano Today* **2022**, *43*, 101428.
[61] J. Gao, B. Liu, *ACS Mater. Lett.* **2020**, *2*, 1008.
[62] M. M. Montemore, M. A. van Spronsen, R. J. Madix, C. M. Friend, *Chem. Rev.* **2018**, *118*, 2816.